RSC Advances

PAPER

View Article Online
View Journal | View Issue

Cite this: *RSC Adv.*, 2024, **14**, 16661

Beyond the ordinary: exploring the synergistic effect of iodine and nickel doping in cobalt hydroxide for superior energy storage applications†

Sheraz Yousaf,[a] Sonia Zulfiqar,[bc] Muhammad Usman Khalid,[a] Muhammad Farooq Warsi,*[a] Imran Shakir,[d] Muhammad Shahid,[e] Iqbal Ahmad*[f] and Eric. W. Cochran*[c]

This study explores the iodine and nickel-doped cobalt hydroxide (I & Ni-co-doped-$Co(OH)_2$) as a potential material for energy storage and conversion applications owing to its excellent electrochemical characteristics. According to our analysis, it was revealed that this material exhibits pseudocapacitive-like behavior, as evident from distinct redox peaks observed in cyclic voltammetry, which confirms its ability to store charges. The diffusion coefficient analysis reveals that this material possesses conductivity and rapid diffusion kinetics, making it particularly advantageous compared to materials synthesized in previous studies. Charge–discharge measurements were performed to analyze the charge storage capacity and stability of this material after 3000 consecutive cycles, showing its excellent stability with minimum loss of capacitance. Furthermore, its anodic and cathodic linear sweep voltammetry curves were measured to evaluate its oxygen evolution and hydrogen evolution reaction performance. The results showed that the material exhibited an excellent water splitting performance, which suggests its potential practical application for hydrogen production. This increased activity was attributed to the doping of α-$Co(OH)_2$, which improved its structural stability, electrical conductivity, and charge transfer efficiency. Thus, I & Ni-co-doped-$Co(OH)_2$ possesses enhanced properties that make it an excellent material for both energy storage and hydrogen generation applications.

Received 12th March 2024
Accepted 5th May 2024

DOI: 10.1039/d4ra01907e

rsc.li/rsc-advances

1 Introduction

In the dynamic and fluctuating environment of energy technologies globally, the development of environmentally friendly solutions for energy storage and water-splitting applications has become increasingly important.[1–3] Consequently, it is necessary to employ renewable energy sources and store their energy for later use.[4–7] This has led to the development of advanced systems that address both problems simultaneously. Additionally, the intermittent nature of power from renewable energy sources makes storage systems such as batteries and supercapacitors crucial for power management.[8,9]

In the case of energy storage, electrocatalytic water-splitting technology involves the production of hydrogen.[10] Hydrogen is an energy source that can be stored for long periods, which is considered a reasonable alternative to conventional fuels. However, traditional methods for the generation of green hydrogen, such as steam methane reforming, are obviously harmful to the environment, and thus not aligned with sustainability. In contrast to proton exchange membrane water splitting, electrocatalytic water splitting employs electricity to directly convert water into hydrogen and oxygen. This technology shows great potential given that it can help avoid the global decline in fuel reserves in the transport and industrial sectors, together with reducing the release of greenhouse gases.[11]

Platinum, iridium oxide (IrO_2), and ruthenium oxide (RuO_2) are a few examples of compounds derived from metals that have been applied as cutting-edge catalysts for HER and OER.[12,13]

---

[a] *Institute of Chemistry, Baghdad-ul-Jadeed Campus, The Islamia University of Bahawalpur, Bahawalpur, 63100, Pakistan. E-mail: farooq.warsi@iub.edu.pk*
[b] *Department of Chemistry, Faculty of Science, University of Ostrava, 30. Dubna 22, Ostrava 701 03, Czech Republic*
[c] *Department of Chemical and Biological Engineering, Iowa State University, Sweeney Hall, 618 Bissell Road, Ames, Iowa 50011, USA. E-mail: ecochran@iastate.edu*
[d] *Department of Physics, Faculty of Science, Islamic University of Madinah, Madinah 42351, Saudi Arabia*
[e] *Department of Chemistry, College of Science, University of Hafr Al Batin, P. O. Box 1803, Hafr Al Batin, 31991, Saudi Arabia*
[f] *Department of Chemistry, Allama Iqbal Open University, Islamabad, 44000, Pakistan. E-mail: Iqbal.ahmad@aiou.edu.pk*

† Electronic supplementary information (ESI) available: Characterization details, chemical equations, preparation of electrode materials, FTIR spectra of electrocatalysts (Fig. ES1), BET plots of the prepared electrocatalysts (Fig. ES2), graph between peak current to the square root of the scan rate (Fig. ES3), graph for percentage contribution of capacitive and diffusion-controlled processes (Fig. ES4), electrochemical active surface area of the prepared materials (Fig. ES5) and preliminary electrochemical experimental parameters (Table ES1). See DOI: **https://doi.org/10.1039/d4ra01907e**

However, the application of these precious metals presents challenges due to their scarcity and limited stability. Thus, the large-scale production of devices and their integration into practical applications face various challenges including high cost and potential risks.[14,15] Additionally, the manufacturing processes for iridium oxide and ruthenium oxide often involve harsh conditions and high temperatures, making their use less practical. Therefore, it is crucial to investigate catalysts that are more cost-effective and capable of long-term usage.[16]

Transition metal-based materials have attracted interest as alternatives to pure metal catalysts due to their mechanical and electrochemical strength,[17,18] and their exceptional reactivity, durability, and abundant availability make them suitable choices as catalysts.[19,20] Furthermore, their properties can be tailored by adopting different strategies such as alloying,[21] forming heterostructures with other potential materials,[22,23] tailoring their morphology[24] and doping with other suitable elements. Among the transition metal-based materials, the characteristics of cobalt-based materials make them appropriate candidates for catalytic applications, providing a viable solution to reduce the dependence on precious metals.[25] Furthermore, cobalt-based catalysts can be synthesized using simple and scalable methods, which can reduce their production costs and facilitate their large-scale application. Compared to the recently reported Co-based catalysts, the significantly lower overpotential of 260 mV at 10 mA cm^{-2} was achieved by incorporating Au in Co-based nanosheets. The improved OER activity of the extremely active Au–Co(OH)$_2$ electrocatalyst is attributed to the direct formation of O–O bonds with the lattice oxygen in Au-doped Co-based nanosheets.[26] Thus, the numerous benefits offered by hybrid catalysts have motivated the investigation of CeO$_2$/Co(OH)$_2$ hybrids. Outstanding OER and HER catalytic activity was achieved by evenly connecting CeO$_2$ nanoplates with Co(OH)$_2$, which resulted in a decrease in overpotential (410 mV and 317 mV, respectively) and Tafel slope (66 mV dec^{-1} for OER and 140 mV dec^{-1} for HER).[27]

OER electrocatalysis was improved by modifying the β-Co(OH)$_2$ surface active sites. Consequently, a low overpotential of 390 mV at 10 mA cm^{-2} and a Tafel slope of 57 mV dec^{-1} were obtained utilizing a single-step bipolar electrochemical method to evaluate the enhanced electrocatalytic activity of the as-synthesized Co(OH)$_2$ nanostructures. However, the high overpotential, limited activity, instability and high cost of cobalt-based electrocatalysts hinder their application in water splitting.[28] Alternatively, cobalt metal was employed in the production of a cost-effective and highly efficient solar-driven electrolyzer (denoted as Co(OH)$_2$/NF). This electrolyzer demonstrated an overpotential of 182 mV for the HER and 281 mV for the OER.[29] A 2D ultrathin α-Co(OH)$_2$ nanosheet catalyst was produced for OER, which exhibited excellent stability and cost-effectiveness in alkaline medium. This catalyst efficiently catalyzed the development of oxygen and the conversion of electrical energy to chemical energy, despite its low Tafel slope and overpotential of 278 mV.

Metallic doping enhances the conductivity and structural stability of materials, contributing to improved charge storage capacity. Alternatively, non-metallic co-doping can tailor the electronic properties and introduce catalytic activity in materials, optimizing their charge transfer kinetics.[30,31] In this case, the combination of metallic and non-metallic dopants yields a comprehensive enhancement in properties, providing versatility and tunability for diverse electrochemical applications.[32] The study by Kou *et al.* on integrated electrodeposition on carbon fabric revealed the superior electrocatalytic performance of Co(OH)$_2$ doped with chlorine due to the increase in the surface area of the electrode.[33] Iodine doping improved the electrical properties of CuO semiconductor films, resulting in an increase in Hall mobility, lower resistance, and improved thin-film transistor performance.[34] A study analyzed the synthesis of nickel hydroxide nanoparticles doped with iodine using a simple hydrothermal method, focusing on their performance in the OER.[35] I-BWO, a Bi$_2$WO$_6$ photocatalyst doped with iodine, outperformed pure BWO and I$_2$-BWO in the degradation of rhodamine B due to its smaller crystalline dimensions, limited energy gap, and abundant oxygen vacancies.[36] A 2D NiCo LDH electrocatalyst with iodine, low resistance to charge transfer, and long-term stability was synthesized using the precipitation technique, indicating potential for efficient energy conversion.[37] Another study presented the synthesis of Co–Ni–Fe511 nanosheets for OER, demonstrating an exceptional performance with a low Tafel slope, minimal degradation, and low energy consumption.[38] Co-doping iodine and nickel in CdS nanostructures yielded thinner, high-crystal CdS nanobelts, indicating the successful integration of the dopants and potentially advancing the development of solar cells and optoelectronic devices.[39] Porous triazine-based frameworks doped with iron and iodine showed enhanced oxygen reduction reaction activity, suggesting a potential synthesis-engineering approach for developing electrocatalysts without platinum.[40]

The aim of the present study is to provide a straightforward precipitation approach for the synthesis of I and Ni co-doped-Co(OH)$_2$ nano-flowers. Ni doping enhanced the electrical conductivity, durability, and catalytic activity of α-Co(OH)$_2$. Meanwhile, iodine doping altered the electronic characteristics of α-Co(OH)$_2$, resulting in an improved electrochemical performance, greater durability, and reduced surface passivation. Moreover, the synergistic effects resulting from the co-doping of Ni and iodine improved the performance of α-Co(OH)$_2$ in terms of energy storage and conversion. The prepared electrocatalysts demonstrated a reduced overpotential in achieving a desirable geometric current density and higher specific capacitance compared to their counterparts. This simple template-free-based method shows promise for the synthesis of amorphous metal hydroxides or oxides for energy storage and conversion applications.

2 Experimental

2.1 Materials

Cobalt nitrate hexahydrate (Co(NO$_3$)$_2$·6H$_2$O, 98% purity), nickel nitrate hexahydrate (Ni(NO$_3$)$_2$·6H$_2$O, 99.999% purity), potassium iodide (KI, ≥99.0% purity), potassium hydroxide (KOH, ≥85% purity), iodine (I$_2$, ≥99.99% purity) and NH$_3$ solution

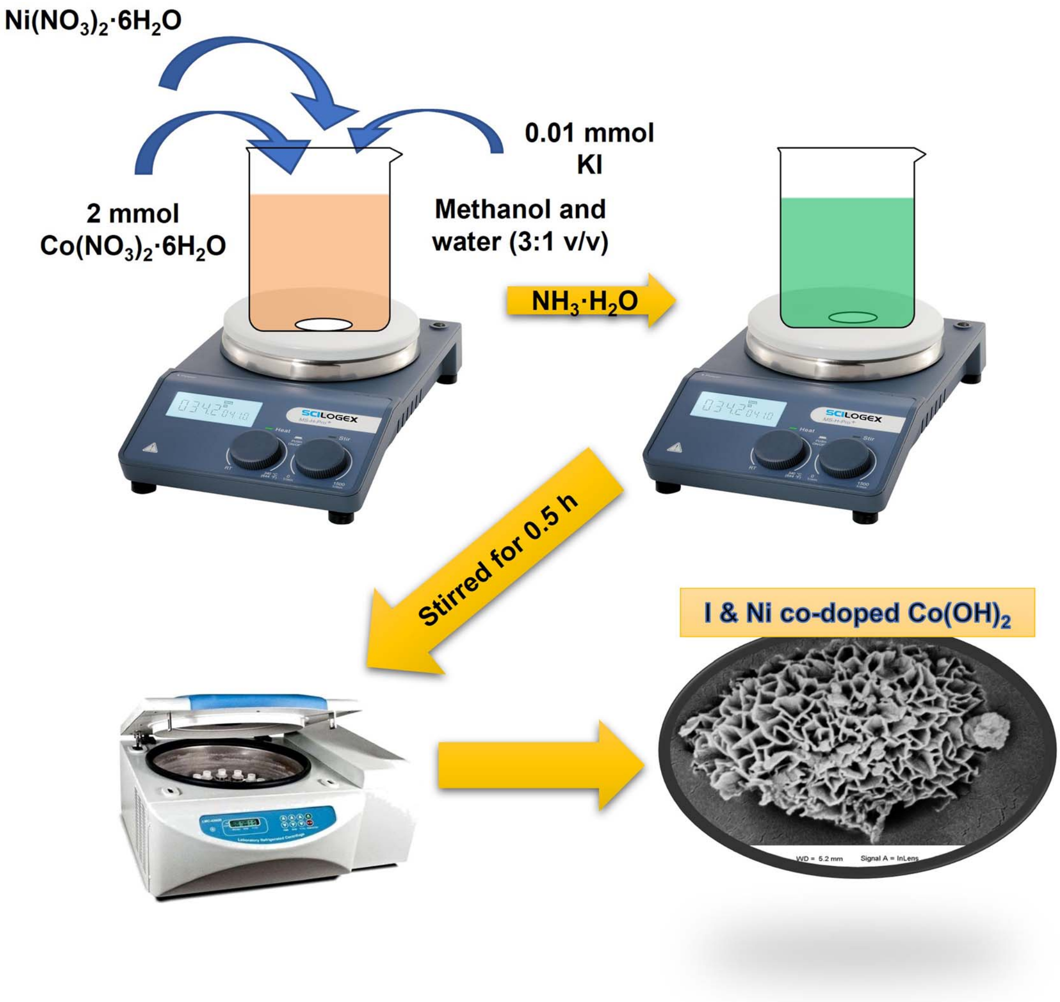

Fig. 1 Schematic illustration of the synthesis of I & Ni-co-doped-Co(OH)$_2$ and I$_2$-loaded Ni-doped-Co(OH)$_2$ through the simple precipitation route.

(25% purity) were purchased from Sigma Aldrich. Methanol (≥99.8% purity) and ethanol 85–87% purity) were obtained from BDH. All chemicals were used as received without further purification.

2.2 Synthesis of electrocatalysts

A solution of 2 mmol of Co(NO$_3$)$_2$·6H$_2$O was prepared in a 3 : 1 (v/v) mixture of methanol and water with a total volume of 15 mL. Then, 300 μL of an NH$_3$ solution was added to a 3 : 1 (v/v) methanol/water solution with magnetic stirring. Following a 30 min incubation period at ambient temperature, a homogeneous colloidal solution with a green hue was observed. The green α-Co(OH)$_2$ precipitate was obtained by the separation of the components of the colloid through centrifugation, followed by air-drying. The inclusion of Ni(NO$_3$)$_2$·6H$_2$O or both Ni(NO$_3$)$_2$·6H$_2$O and KI in the aforementioned procedure led to the formation of Ni-doped Co(OH)$_2$ and I & Ni co-doped Co(OH)$_2$, respectively. Subsequently, the prepared Ni-doped Co(OH)$_2$ was mixed with 16 mg alcoholic solution of pure iodine in a mortar and pestle to prepare the blank or reference material for comparative analysis with our doped samples, which was denoted as I$_2$-loaded Ni-doped-Co(OH)$_2$. This approach aimed to create a baseline material for analyzing and comparing the properties of the doped samples. The synthesis process is schematically shown in Fig. 1.

3 Results and discussion

3.1 Structural analysis

Powder X-ray diffraction (XRD) is a well-established technique widely utilized to gain valuable insights into the properties of materials such as their composition and structure. As a non-destructive tool, XRD is often used for determining the crystalline structure of materials, such as powdered samples. Thus, in the current investigation, XRD was implemented to analyze and determine the structural attributes of the various electrocatalysts, including α-Co(OH)$_2$, Ni-doped-Co(OH)$_2$, I & Ni co-doped-Co(OH)$_2$, and I$_2$-loaded Ni-doped-Co(OH)$_2$, and the results are depicted in Fig. 2. The diffraction pattern of cobalt

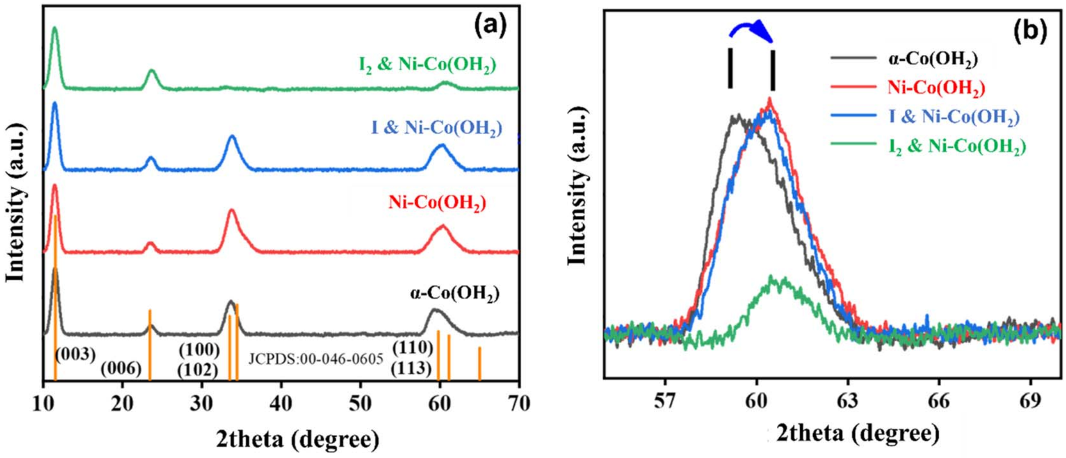

Fig. 2 (a) XRD patterns of various electrocatalysts, α-Co(OH)$_2$, Ni-doped-Co(OH)$_2$, I & Ni-co-doped-Co(OH)$_2$, and I$_2$-loaded Ni-doped-Co(OH)$_2$. (b) Impact of doping on diffraction peaks shown by the phenomenon of peak shifting.

hydroxide displayed peaks at 2θ values of 11.3°, 23.1°, 33.5°, 34.6°, 59.3°, and 61.1°, which correspond to the (003), (006), (100), (102), (110) and (113) diffraction planes (JCPDS: 046-0605). The nickel-doped, iodine & nickel co-doped, and I$_2$-loaded Ni-doped Co(OH)$_2$ electrocatalysts were analyzed, and no additional diffraction peaks were detected in their XRD patterns, confirming the homogeneity of these material. Alternatively, a shift in the (110) diffraction peak of Ni-doped-Co(OH)$_2$ and Ni-doped Co(OH)$_2$ co-doped with iodine and nickel was observed, as illustrated in Fig. 2(b). The observed phenomenon of shifting is believed to be a result of the homogeneous incorporation of the Ni dopant in the lattice structure of α-Co(OH)$_2$. The addition of nickel as a dopant can cause changes in the arrangement of the crystal lattice because Ni^{2+} ions have a smaller radius (0.69 Å) compared to Co^{2+} ions (0.79 Å). Moreover, distinguishing between the two phases of α-Co(OH)$_2$ and Ni(OH)$_2$ can be challenging due to the similarity of their diffraction patterns.[41]

However, considering nickel and iodine co-doped α-Co(OH)$_2$, it is possible that iodine may fill the spaces between the layers of alpha cobalt hydroxide due to its suitable size (ionic radius of 2.2 Å). Specifically, alpha cobalt hydroxide has an interlayer spacing of 7 Å, which should be sufficient to accommodate iodine ions. However, the potential impact of the presence of iodine in the interlayer spaces of alpha cobalt hydroxide in terms of its stability and reactivity need to be explored, especially considering its potential use as a catalyst or electrode material.[42]

The Debye Scherrer formula was used to determine the size of the crystallite particles in the materials. Our analysis revealed that the sizes of α-Co(OH)$_2$, Ni-doped Co(OH)$_2$, iodine and nickel co-doped Co(OH)$_2$, and I$_2$-loaded Ni–Co(OH)$_2$ were 14 nm, 7.1 nm, 7.2 nm, and 6.8 nm, respectively. The decrease in crystallite size can be attributed to the inclusion of iodine in the structure of the α-Co(OH)$_2$ electrocatalysts given that it hinders the formation of crystals by interfering with the crystal growth process. Ultimately, this leads to the formation of crystallites.[43] Additionally, potassium iodide can act as a catalyst, encouraging the development of crystalline structures. The iodide ions can assist in the creation of crystal formations and boost the speed at which crystals grow, leading to a greater concentration of smaller crystallites.[35] Also, the presence of KI has an impact on the nucleation process, greatly influencing the dynamics of crystallization. Some of the structural changes that occur include changes in crystal size, morphology, and atomic arrangement within the lattice, all of which have a significant effect on the properties of the material. Thus, the crystallization process and characteristics of the resultant crystals are both modified by the presence of KI, where a higher concentration of smaller crystallites was observed because the iodide ions encouraged the formation of seed crystals and sped up the crystal growth process.[35]

3.2 Fourier transform infrared spectroscopy (FTIR)

Additional analysis was conducted utilizing Fourier transform infrared (FTIR) spectroscopy, a methodology that facilitates the detection of molecular vibrations within a material and confirms the existence of lattice oxygen, crystalline water, and interlayer anions. The FTIR methodology produces a clear and precise depiction of the molecules present in a sample, making it an essential tool. The FTIR spectra of the produced compositions are presented in Fig. ES1.† The spectral pattern observed at around 3457 cm^{-1} is associated with the stretching vibration of O–H bonds, which are related to the presence of OH groups and water molecules inside the intermolecular environment.

This intrinsic factor ultimately removes the inherent charge of nickel and cobalt, making the structural framework neutral.[44] Moreover, the band that appeared at the wavenumber of 1625 cm^{-1} belongs to the bending mode of the water molecules, which is present throughout the framework.[45] The presence of methanol molecules in the interlayers was proven by the appearance of weak bands at 1090, 2919, and 2816 cm^{-1}, corresponding to the C–H and C–O vibrations.[46] In addition, the observed bands in the range of 500 to 600 cm^{-1} correspond to

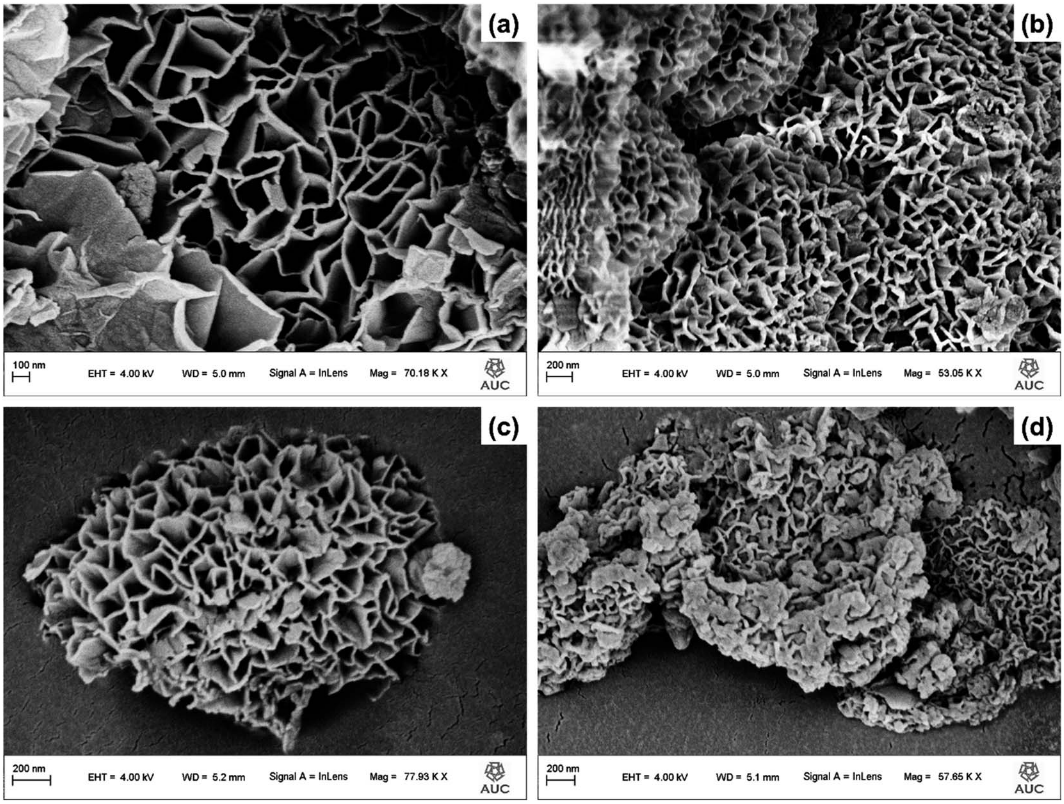

Fig. 3 FESEM images of different electrocatalysts (a) α-$Co(OH)_2$, (b) Ni-doped-$Co(OH)_2$, (c) I & Ni-co-doped-$Co(OH)_2$, and (d) I_2-loaded-Ni-doped-$Co(OH)_2$.

the bond vibrations of Ni O–M and O–M–O, where M represents the chemical elements Ni and Co.[47] The change in the bands of α-$Co(OH)_2$ due to addition of Ni or both Ni and iodine in the FTIR spectra demonstrate the change in the molecular framework and the unique nature of the chemical bonds and vibrational modes of the material, and also the change in its local structure.

3.3 Morphological investigations

3.3.1 ***Field emission scanning electron microscopy (FESEM)*** **analysis.** The surface morphology of an electrocatalyst greatly influences its reaction performance. Thus, we studied the surface structure of the prepared electrocatalysts including α-$Co(OH)_2$, Ni-doped-$Co(OH)_2$, I & Ni co-doped-$Co(OH)_2$ and I_2-loaded-Ni-doped-$Co(OH)_2$ using field emission scanning electron microscopy (FESEM), as depicted in Fig. 3. The images provided evidence of the existence of discrete three-dimensional nano-flowers within the α-$Co(OH)_2$ electrocatalyst, where the nano-flowers were composed of nanosheets. The presence of nanoflowers on the surface of the α-$Co(OH)_2$ electrocatalyst enhanced its activity. This enhancement is attributed to the increased active surface area and improved charge transfer efficiency facilitated by the nano-flowers. From a morphological standpoint, it can be observed that Ni-doped-$Co(OH)_2$, I & Ni-co-doped-$Co(OH)_2$, and their counterparts exhibit considerable similarities. However, it is worth noting that variations in their thickness are evident. The morphology of the Ni-doped-$Co(OH)_2$ electrocatalyst subjected to I_2 loading was similar to that of the precursor without any loading. In contrast, it showed signs of agglomeration and a higher liquid content within its voids. However, these modifications were insufficient to address or alleviate the presence of cracks.[48] The distinctive form of the material under consideration afforded a substantial surface area, facilitating the presence of a greater number of active sites for the electrochemical process. Consequently, this enhanced its activity, which led to better efficiency. Moreover, the 3D structure resembling a flower can boost the movement of substances, improving the dispersion of the reactants and products and reducing the differences in potential.[49] Additionally, this exclusive flower-like shape enhanced the stability and long-term durability of the catalyst during the energy storage and conversion processes, which helped to minimize its degradation over time.

3.3.2 Transmission electron microscopy (TEM) analysis. TEM is an imaging method that utilizes electrons to examine the internal structure of materials at a nanoscale resolution. In the field of materials science and electrochemistry, TEM plays a role in uncovering details about material properties. By providing insights into the morphology of materials, TEM contributes to the development of materials for various electrochemical applications. The TEM images, as shown in Fig. 4, reveal the presence of defined 3D nanostructures within the α-$Co(OH)_2$ electrocatalyst. These nanostructures bear a striking resemblance to the nanoflowers observed in the FESEM

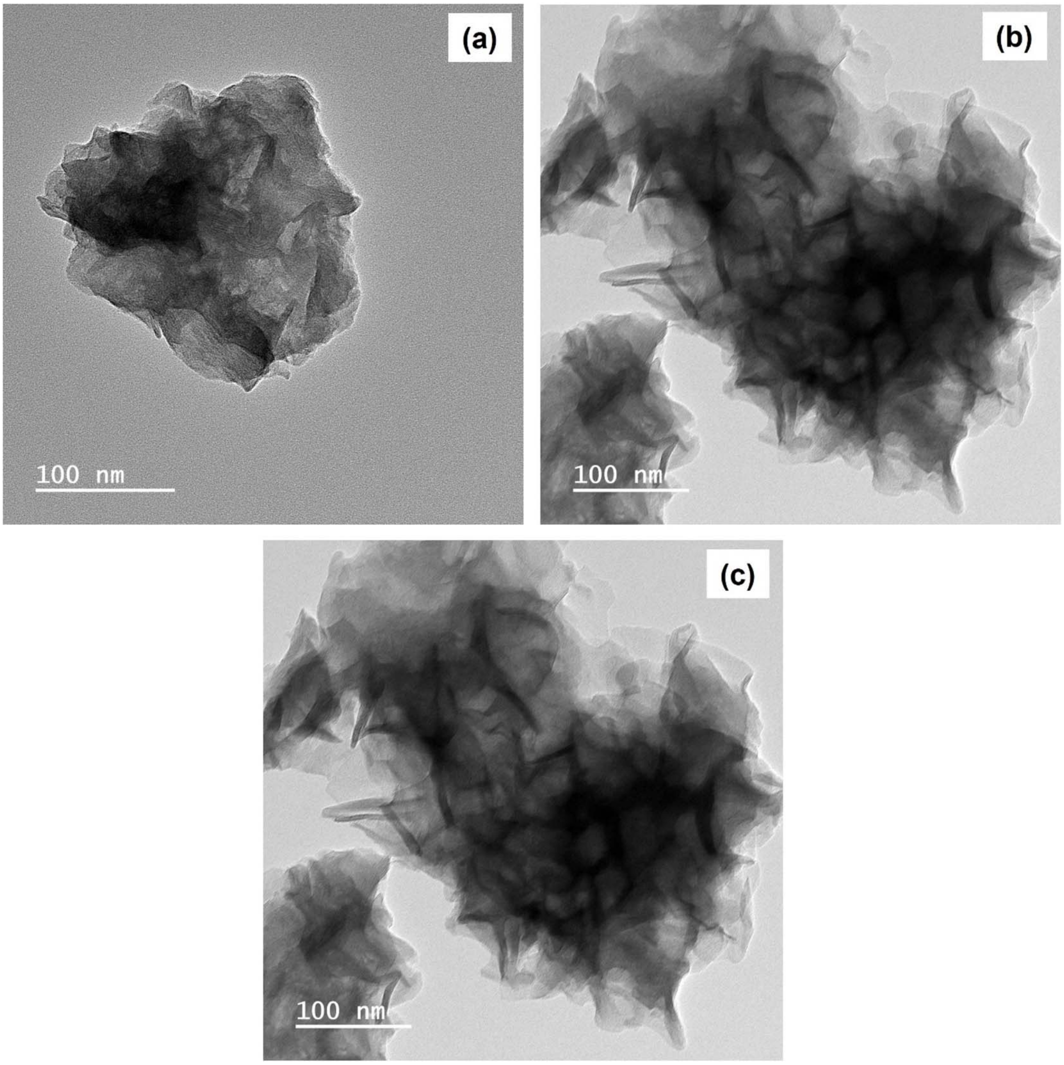

Fig. 4 TEM images of (a) α-$Co(OH)_2$, (b) Ni-doped-$Co(OH)_2$, and (c) I & Ni-co-doped-$Co(OH)_2$.

analysis. The thin layers forming these nanostructures are helpful in enhancing activity by increasing the surface area and facilitating efficient charge transfer, which explains the observed improvements in electrochemical performance.

It is worth noting that the TEM analysis highlighted similarities among Ni-doped-$Co(OH)_2$, I & Ni-co-doped-$Co(OH)_2$, and their pristine counterparts, which are consistent with the FESEM observations. However, noticeable differences in thickness are apparent, underscoring the sensitivity of TEM to capture distinctions. Moreover, the flower-like structure, as determined by TEM, significantly contributed to the stability and durability of the catalyst during the energy storage and conversion processes.

3.4 BET analysis

Enhancing the surface area of a material is a viable strategy for improving its electrochemical performance. Accordingly, N_2 gas adsorption–desorption studies were performed to determine the surface area of the designed materials. The present investigation evaluated the BET adsorption–desorption isotherms of the α-$Co(OH)_2$ materials that were subjected to doping with Ni or co-doping with Ni and I. The results revealed that the samples displayed type IV isotherms accompanied by H_3 hysteresis loops. The objective of this study was to ascertain the surface area of Ni-doped-$Co(OH)_2$ and I & Ni-co-doped-$Co(OH)_2$, which was determined to be 12.859 $m^2\ g^{-1}$ and 20.094 $m^2\ g^{-1}$, respectively. The observed enhancement in the surface area of the co-doped sample can be attributed to the comparatively porous structure of the α-$Co(OH)_2$ material, as validated by the FESEM images. However, simply possessing an increased surface area does not guarantee enhanced electrochemical effectiveness. Specifically, the presence of a sufficient quantity of reservoirs that possess the capacity to retain water molecules or electrolytic species is crucial for sustaining the catalytic activity. Thus, the pore diameter and pore area of the samples were also considered, as illustrated by the bar graphs in the

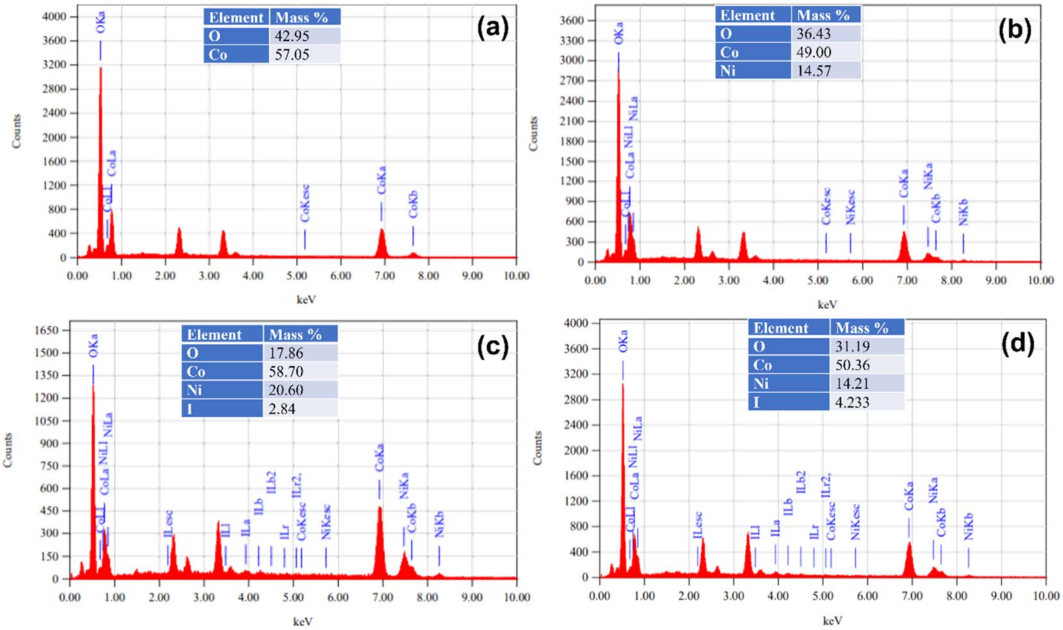

Fig. 5 EDX spectra of several electrocatalysts (a) α-$Co(OH)_2$, (b) Ni-doped-$Co(OH)_2$, (c) I & Ni-co-doped-$Co(OH)_2$, and (d) I_2-loaded-Ni-doped-$Co(OH)_2$.

inset of Fig. ES2.† The reduction in the pore size of Ni-doped-$Co(OH)_2$ was concurrent with a reduction in its pore diameter, whereas the opposite trend was observed for the α-$Co(OH)_2$ co-doped with I and Ni sample. In this instance, the increase in pore area resulted from the reduction in pore diameter, indicating the presence of more penetrating pores with a higher capacity to retain electrolytic species. The resultant trend can be ascribed to the synergistic effect of the dopants, which improved the electrochemical performance.

3.5 Elemental analysis

EDX analysis is an effective method employed to determine the elemental constitution of a substance through the detection and examination of X-rays emitted from it upon being subjected to electron bombardment. The EDX results of α-$Co(OH)_2$, Ni-doped-$Co(OH)_2$, I & Ni-co-doped-$Co(OH)_2$, and I_2-loaded-Ni-doped-$Co(OH)_2$ are shown in Fig. 5, which confirm the presence of all the expected elements within the designed electrocatalysts. Both cobalt and oxygen were detected in the EDX spectrum of α-$Co(OH)_2$, while cobalt and nickel were also detected in the EDX spectrum of Ni-doped $Co(OH)_2$, indicating the successful doping of Ni in the $Co(OH)_2$ lattice. Moreover, both Ni and iodine were also detected in Ni-doped-$Co(OH)_2$ loaded and doped with iodine. This confirmed the successful incorporation of both Ni and iodine within the lattice of α-$Co(OH)_2$. Moreover, a significant content of iodine was also detected, as shown in tabular form in Fig. 5.

3.6 X-ray photoelectron spectroscopy

X-ray photoelectron spectra were recorded to analyze the surface compositions and chemical states of the as-prepared α-$Co(OH)_2$, Ni-doped-$Co(OH)_2$, and I & Ni-co-doped-$Co(OH)_2$ samples, as shown in Fig. 6. The XPS analysis of I & Ni-co-doped-$Co(OH)_2$ showed the presence of Co, Ni, O, I, and C elements. The binding energies from XPS analysis were analyzed using the CasaXPS software. Fig. 6(a–c) show the high-resolution XPS spectra of the C 1s orbit with a peak at 284.6 eV, which is attributed to the surface amorphous carbon of the reference C 1s from the XPS instrument.[50] The O 1s core-level spectrum of all the synthesized samples in this study showed a peak at the binding energy of approximately 532 eV, as shown in Fig. 6(d–f). This suggests that the oxygen species are attributed to lattice oxygen ions and hydroxyl oxygen on the surface. The O 1s XPS spectra show two peaks, one at 530.5 eV, indicating the presence of hydroxide in α-$Co(OH)_2$, and a smaller peak at 533.1 eV, indicating the presence of adsorbed water.[51]

Fig. 6(g–i) show the measured high-resolution XPS spectra of Co 2p for all the synthesized samples. The Co 2p XPS spectra display two main peaks at 779.1 and 794.9 eV, which correspond to Co $2p_{3/2}$ and $2p_{1/2}$, respectively. The spin-energy separation of 15.8 eV indicates the presence of Co^{2+}. Two satellites of Co $2p_{2/3}$ and Co $2p_{1/3}$ were observed at 784.1 and 801.0 eV, respectively, confirming the formation of the α-$Co(OH)_2$ phase.[52] Ni-doped $Co(OH)_2$ showed four distinct peaks in the Ni 2p region. These peaks correspond to Ni $2p_{3/2}$ and Ni $2p_{1/2}$ with binding energies of 855.2 eV and 873 eV, respectively, together with a satellite peak, suggesting that nickel exists in the bivalent state. Fig. 6(j and k) show the XPS Ni 2p core-level spectra.[38]

The I 3d core-level spectrum showed two peaks at 631.8 eV and 620.5 eV, corresponding to I $3d_{3/2}$ and I $3d_{5/2}$, respectively (see Fig. 6(l)). These peaks differed from the binding energies of 630.1 and 619.1 eV observed for the characteristic bands of iodine in I_2. The peak at 619.1 eV is due to the negatively charged iodine (I^-) species, while the peak at 630.1 eV is

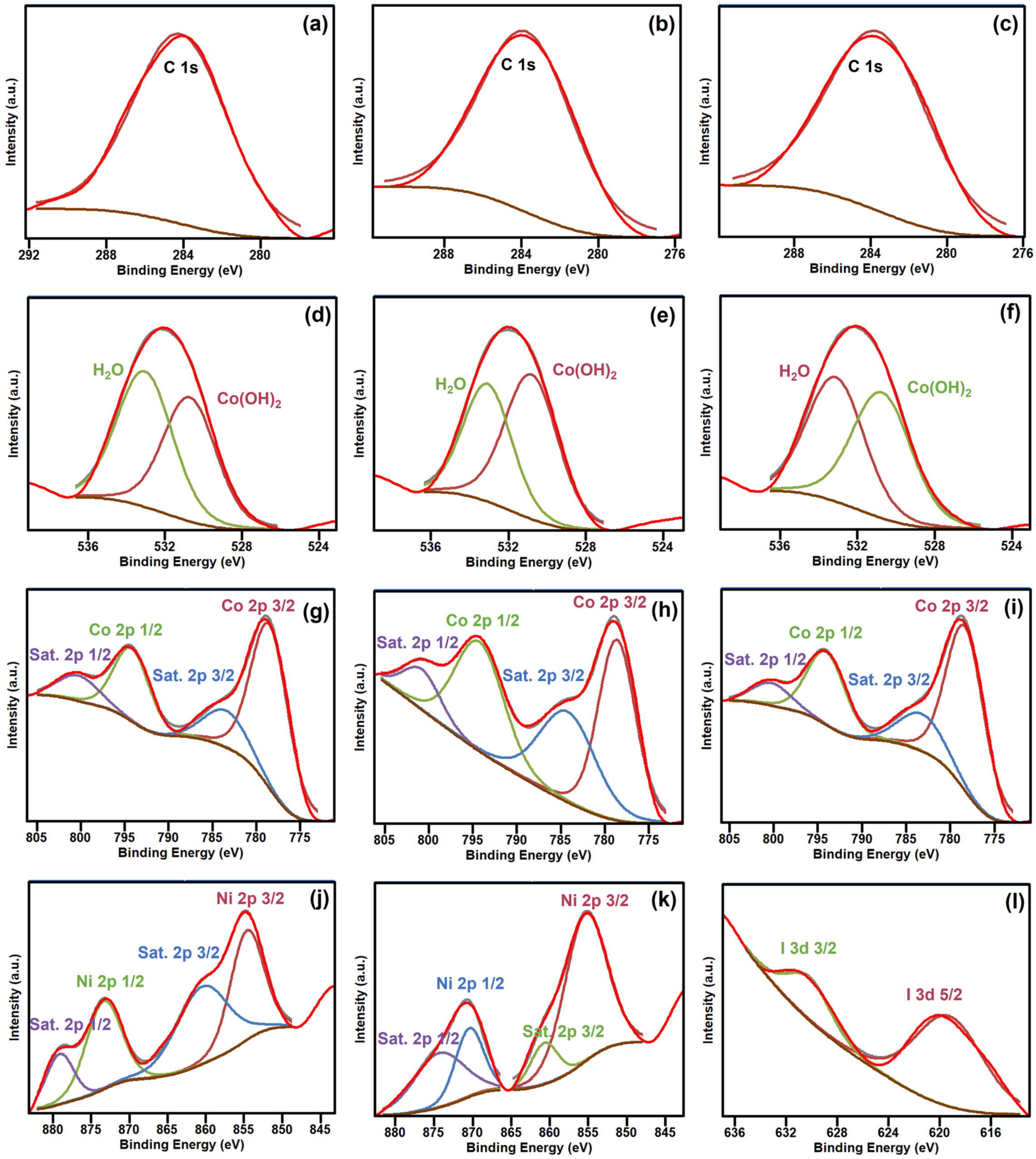

Fig. 6 XPS C 1s (a–c), O 1s (d–f), Co 2p (g–i), Ni 2p (j and k) and I 3d (l) spectra of as-prepared α-$Co(OH)_2$, Ni-doped-$Co(OH)_2$ and I & Ni-co-doped-$Co(OH)_2$ electrocatalysts, respectively.

attributed to I_2.[53] The surface adsorption of α-$Co(OH)_2$ caused a chemical shift of approximately 1.0 eV for I_2. The I^- ions may react to form I_2 during synthesis according to the following reaction: $4I^- + O_2 + 4H^+ \rightarrow 2I_2 + 2H_2O$.[36]

3.7 Energy storage applications

Energy storage plays an indispensable role in technology given that it allows the effective utilization of energy sources and development of portable electronics and electric vehicles. In this case, the progress achieved herein can contribute to the development of suitable materials, indicating a significant advancement in addressing existing limitations and marking a new era for energy storage and its vital role in our energy ecosystem. We analyzed the suitability of α-$Co(OH)_2$, Ni–$Co(OH)_2$ and I & Ni-co-doped-$Co(OH)_2$ for application in energy storage and electrochemical water splitting. We investigated the behavior of these materials by performing cyclic voltametric (CV) studies in a 1 M KOH solution at various scan rates ranging from 1 to 100 mV s^{-1}.[54] The CV curves obtained during this study (Fig. 7(a–c)) clearly showed peaks for all the materials, indicating their pseudocapacitive behavior. This behavior is advantageous for energy storage given that it enables the accumulation of charge through faradaic redox reactions occurring at the interface between the electrode and electrolyte.

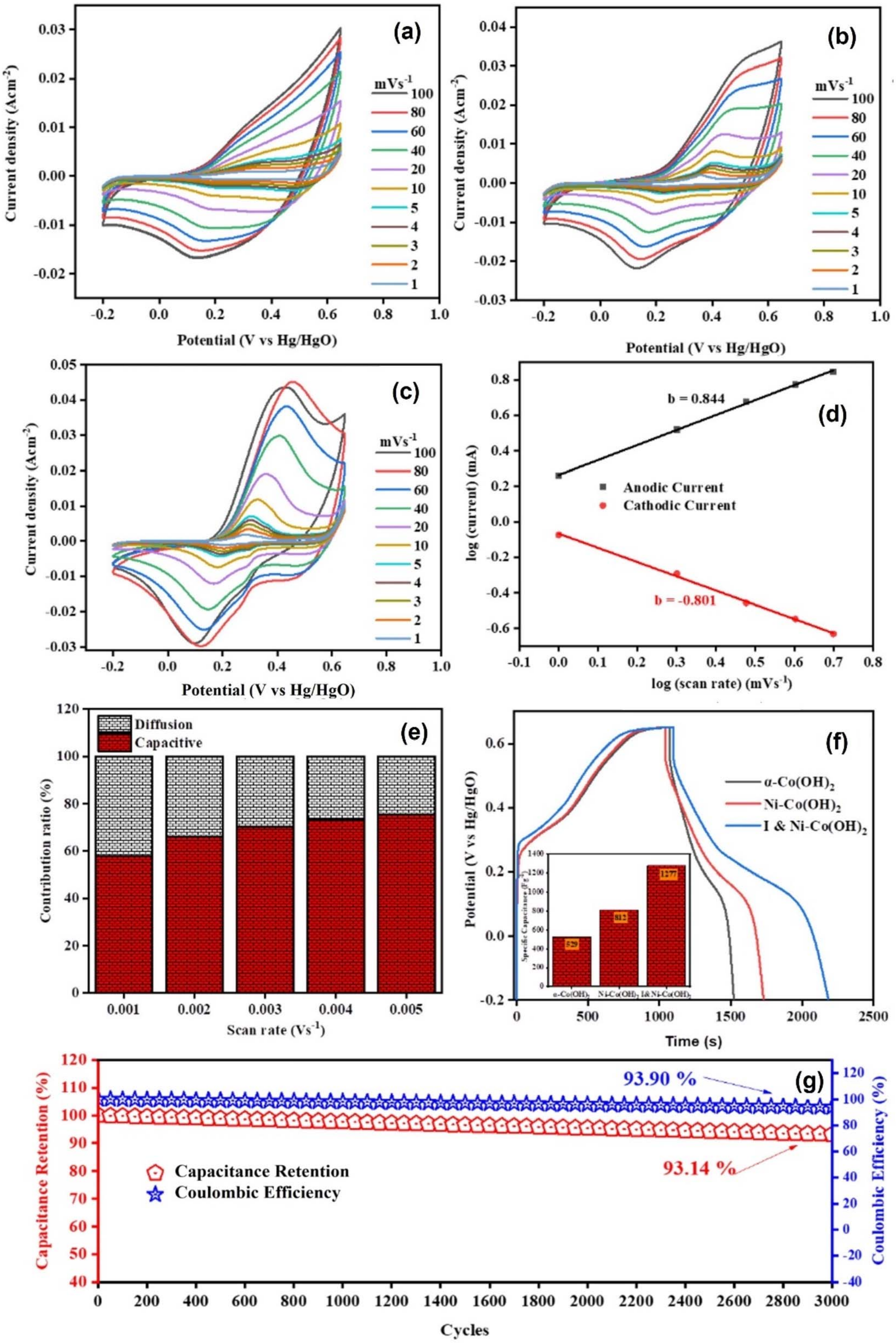

Fig. 7 Cyclic voltammograms (a–c) and graphical representation of anodic and cathodic peak currents *vs.* logarithm of the scan rate (d) for α-$Co(OH)_2$, Ni-doped-$Co(OH)_2$, and I & Ni-co-doped-$Co(OH)_2$. Bar graph (e) for percentage contribution of diffusion and capacitive processes in the case of I & Ni–$Co(OH)_2$ and (f) GCD curves of α-$Co(OH)_2$, Ni–$Co(OH)_2$, and I & Ni–$Co(OH)_2$. (g) Stability of I & Ni-co-doped-$Co(OH)_2$ for energy storage applications, including capacitance retention and coulombic efficiency retained after 3000 GCD cycles.

Consequently, this results in an improved capacitance for storing energy.

Furthermore, the data suggests that with an increase in the scan rate, the area under the CV curve increased. This discovery provides evidence supporting the existence of faradaic redox processes and pseudocapacitive characteristics in these materials. The ability to effectively store and release charge at different rates is a desirable trait for practical energy storage applications, making these materials highly promising for supercapacitor technology.[55,56] The stronger increase in the area beneath the CV curve for I & Ni-co-doped-$Co(OH)_2$ is consistent with its improved performance, indicating its potential for advanced energy storage applications. The enhanced electronic conductivity resulting from Ni and I doping enables electron transfer, leading to efficient faradaic redox reactions. Additionally, the presence of defects originating from doping offers active sites for charge storage, which are responsible for the increase in capacitance.

The graph of peak current (I_{pa}) *vs.* square root of scan rate was plotted to observe the diffusion-limited mechanism in the synthesized electrodes, as shown in Fig. ES3.† The diffusion coefficients (D) for α-$Co(OH)_2$, Ni-doped-$Co(OH)_2$, and I & Ni-co-doped-$Co(OH)_2$ were found to be 0.00089, 0.00299 and 0.0051, respectively.[57] The highest diffusion coefficient observed for I and Ni co-doped $Co(OH)_2$ suggests the best electrical conductivity and fastest electronic movement within the electrode material, as is evident from the EIS results. Besides, a power law model (eqn ES1†) was used by plotting the graph of the logarithm of the scan rate and current for all the designed electrodes to further investigate the charge storage mechanism across the electrode and electrolyte interface, as shown in Fig. 7(d) and ES4.† The slope of this graph is employed to predict the kinetic constant (b). A b value of 0.5 indicates that the diffusion-limited process is dominant, whereas a value of 1 suggests a surface process as the dominant approach for overall charge storage. The b values for α-$Co(OH)_2$, Ni–$Co(OH)_2$, and I & Ni–$Co(OH)_2$ were determined to be 0.732, 0.575, and 0.844, respectively.

These findings indicate that the synthesized materials have properties that support both diffusion and capacitive-controlled processes, making them suitable for energy storage applications. The kinetic constants are in the range of 0.5 to 1, suggesting a combination of both diffusion and controlled charge storage mechanisms. This is consistent with our results indicating that charge storage occurs through faradaic redox processes at the interface between the electrode and electrolyte. The versatility of these materials in energy storage applications is attributed to their ability to incorporate both diffusion and capacitive-controlled processes, enabling charge storage and release at varying rates.

Moreover, we utilized the Dunn method to calculate the charge contribution (eqn ES2†). These calculations are plotted in Fig. 7(e) and ES4.† It appears that as the rate increased, the diffusion contribution decreased, while the capacitive contribution increased. This behavior can be attributed to the time constraint on the diffusion process. At higher scan rates, the time available for the diffusion of charge carriers within the materials becomes limited, leading to a reduced diffusion contribution. In contrast, the capacitive contribution becomes dominant as it involves rapid capacitive-controlled mechanisms that are less affected by the time constraints imposed by higher scan rates. This observation further reinforces the variation in charge storage mechanism observed earlier, where both diffusion- and capacitive-controlled processes played significant roles in the charge storage at different scan rates.[58]

The galvanostatic charge–discharge (GCD) was studied to further assess the charge storage capabilities of the synthesized materials. Fig. 7(f) illustrates the GCD curves acquired at a current density of 1 A g^{-1}. Notably, the shape of the GCD curves exhibited non-linearity for all the materials, providing further confirmation of the presence of redox reactions, which is consistent with the observations in CV measurements.[59,60] The specific capacitance values ascertained using the GCD tests were found to be 529 F g^{-1} (439 C g^{-1}), 812 F g^{-1} (674 C g^{-1}) and 1277 F g^{-1} (1060 C g^{-1}) for α-$Co(OH)_2$, Ni–$Co(OH)_2$, and I & Ni–$Co(OH)_2$, respectively. Among the materials, I & Ni–$Co(OH)_2$ exhibited the greatest specific capacitance, indicating its superior capacity for electrical charge storage. The observed increase in specific capacitance can be ascribed to the advantageous impacts of cationic and anionic doping, which generate a greater number of active sites for charge storage and facilitate effective charge transport routes inside the material.

Furthermore, the initial coulombic efficiency of the materials was calculated using the GCD data, with values of 41.88%, 66.35%, and 98.5% for α-$Co(OH)_2$, Ni–$Co(OH)_2$, and I & Ni–$Co(OH)_2$, respectively. The impressive initial efficiency of I & Ni-co-doped-$Co(OH)_2$ suggests that it can resist energy loss during the charge and discharge cycles. This indicates the transport of charges and efficient redox reactions in I & Ni-co-doped-$Co(OH)_2$, which contribute to its performance and overall stability.

The reliability and durability of the materials were evaluated through stability tests, where I & Ni-co-doped-$Co(OH)_2$ maintained a capacitance of 93.14% and coulombic efficiency of 93.90% during 3000 consecutive charge discharge cycles. This suggests the excellent stability of the electrode in terms of energy storage, which is attributed to Ni and I doping. Specifically, the Ni and I doping minimized the degradation during charge–discharge cycles, created charge storage sites, and facilitated the charge transfer kinetics, contributing to the long-term stability. However, the slight decrease in performance during 3000 cycles can be attributed to various factors such as surface alteration resulting from prolonged cycling, side reactions, and impurities.

3.8 OER performance

The current study also evaluated the electrocatalytic efficiency of the different electrocatalysts, namely α-$Co(OH)_2$, Ni-doped-$Co(OH)_2$, and I & Ni-co-doped-$Co(OH)_2$, for water oxidation using LSV in a 1 M KOH aqueous solution with iR-compensation (Fig. 8(a)). The findings indicate that α-$Co(OH)_2$ co-doped with I and Ni exhibited a superior electrocatalytic performance compared to the other electrocatalysts synthesized

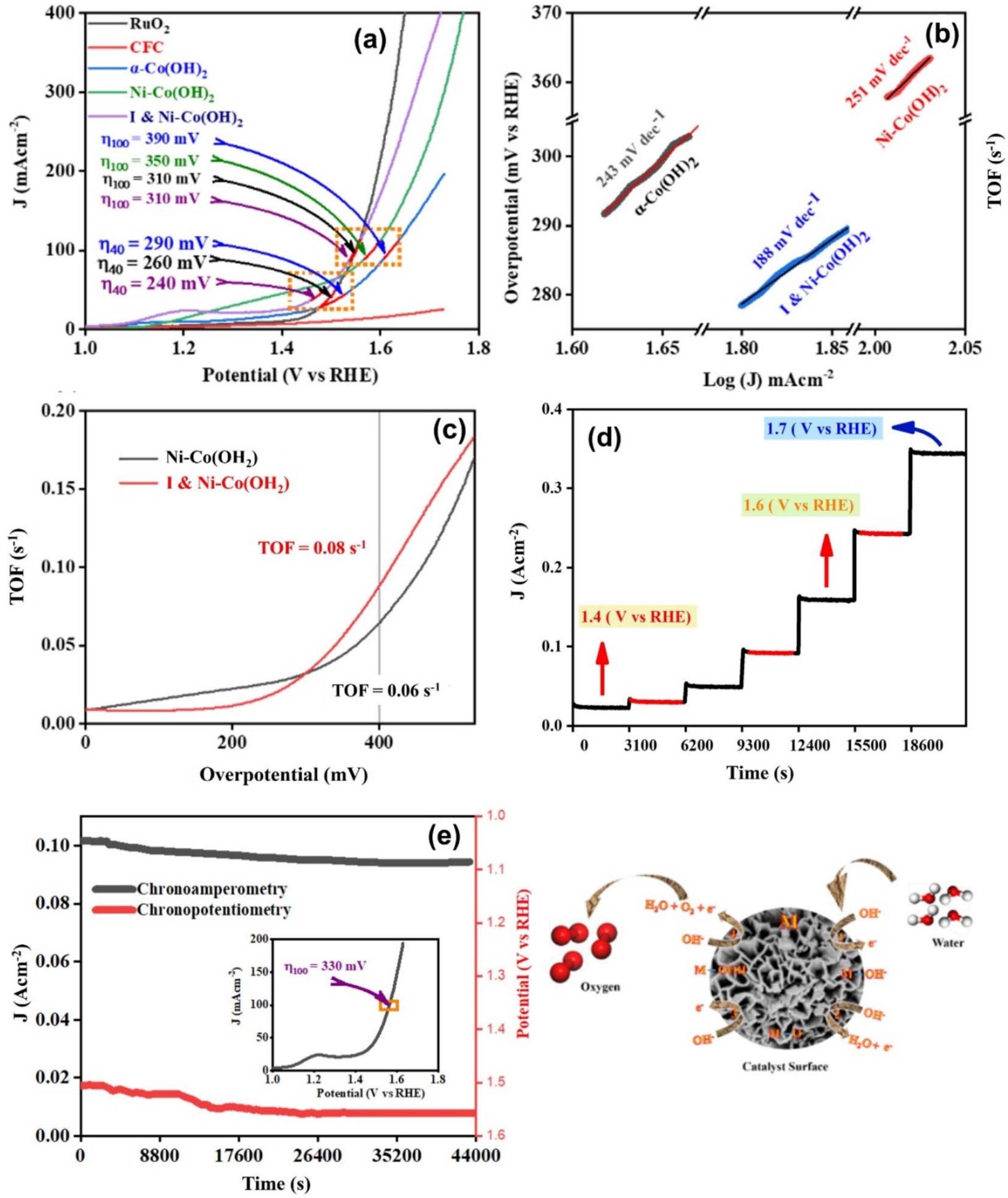

Fig. 8 OER LSV curves (a) and Tafel slopes (b) of various electrocatalysts tested in the current study. (c) Visual depiction of the turnover frequency as a function of the overpotential during the OER for Ni-doped-Co(OH)$_2$ and I & Ni-co-doped-Co(OH)$_2$. (d) Multistep chronoamperometric analysis and (e) long-term chronoamperometric (at 1.55 V vs. RHE) and chronopotentiometric analysis (at 100 mA cm^{-2}) for I & Ni co-doped-Co(OH)$_2$. Inset of (e) depicts the post-LSV analysis results obtained from the stability testing.

under identical conditions. In contrast, the co-doped-Co(OH)$_2$ catalyst exhibited a significantly lower overpotential of 240 mV (*vs.* RHE) to achieve a current density of 40 mA cm^{-2} (η_{40}), whereas the α-Co(OH)$_2$ electrocatalyst necessitated an overpotential of 290 mV (*vs.* RHE). Remarkably, the co-doped-Co(OH)$_2$ catalyst demonstrated an impressive performance, achieving current densities of 100 mA cm^{-2} at 310 mV (*vs.* RHE) and 200 mA cm^{-2} at 340 mV (*vs.* RHE). This suggests that the co-doped-Co(OH)$_2$ electrocatalyst shows promise for energy conversion and storage applications.

The Tafel slope is another measurement utilized for examining the kinetics of reactions. It establishes a connection between the potential and the logarithm of the reaction rate. Several factors such as surface area, surface chemical composition, and crystal structure of electrocatalysts influence the adsorption and release of the reaction intermediates, and consequently have an impact on the Tafel slope. Thus, to examine the kinetics of the OER activity of the electrocatalysts, we also performed a Tafel plot analysis, as depicted in Fig. 8(b). The Tafel slope value of 243 mV dec^{-1} observed for α-Co(OH)$_2$

Table 1 Assessment of the OER experimental parameters for α-$Co(OH)_2$, Ni-doped-$Co(OH)_2$, and I & Ni co-doped-$Co(OH)_2$

S. No.	Material	Onset potential (V *vs.* RHE)	Overpotential (mV) η_{40}	η_{100}	η_{350}	Tafel slope (mV dec^{-1})	TOF@ η_{40} (s^{-1})
1	α-$Co(OH)_2$	1.50	290	390	—	243	—
2	Ni–$Co(OH)_2$	1.50	—	350	520	251	0.06
3	I & Ni–$Co(OH)_2$	1.47	240	310	460	188	0.08

indicates that the reaction kinetics encounter an energy barrier. The efficiency of the electrocatalyst was reduced due to the necessity of an overpotential to maintain the reaction rate, as evident from the Tafel slope.[16] After the addition of Ni during the doping process, it was noticed that the Tafel slope increased to 251 mV dec^{-1}. This indicates that the incorporation of Ni did not improve the reaction kinetics and may create an energy barrier for the reaction,[61] which can be attributed to the changes in the surface chemistry of α-$Co(OH)_2$, leading to a reaction mechanism with a Tafel slope.

In contrast, when both I and Ni were co-doped in the α-$Co(OH)_2$ electrocatalyst, there was an enhancement in the reaction kinetics, as seen from its Tafel slope of 188 mV dec^{-1}, compared to α-$Co(OH)_2$ and Ni-doped-$Co(OH)_2$. The decrease in the Tafel slope suggests that the combined presence of iodine and nickel resulted in a decrease in the activation energy and improvement in the electrocatalytic performance of the catalyst.[62] The improved electrocatalytic efficiency of α-$Co(OH)_2$ when doped with both I and Ni can be attributed to different factors, including the formation of I–Ni–OH species, which act as sites for the desired reaction. Also, changes in the structure of α-$Co(OH)_2$, which facilitate the preferred reaction pathway and modification of the adsorption and desorption properties of the reaction intermediates. During this study, it was observed that the charge transfer coefficient was higher for the electrocatalyst containing I & Ni-co-doped $Co(OH)_2$ compared to the other compositions. This finding is consistent with the performance of the I & Ni-co-doped-$Co(OH)_2$ electrocatalyst in promoting OER. The results suggest that the higher charge transfer coefficient in the I-&-Ni-co-doped-$Co(OH)_2$ electrocatalyst may contribute to its improved electrocatalytic activity.

Furthermore, the turnover frequency (TOF) is employed to evaluate the efficiency of a catalyst assuming that all its metal ions are fully functional, which is calculated using the equation in eqn ES4.†,[63] The results depicted in Fig. 8(c) display the TOF values for the electrocatalysts comprised of Ni-doped-$Co(OH)_2$ and I & Ni-co-doped-$Co(OH)_2$ at an overpotential of 400 mV. This investigation ascertained that the TOF of α-$Co(OH)_2$ doped with Ni is 0.06 s^{-1}. In contrast, the TOF value of α-$Co(OH)_2$ co-doped with I and Ni is 0.08 s^{-1}. This implies that the latter demonstrated a higher catalytic performance in comparison to the former. All the OER experimental parameters are presented in Table 1.

A multistep chronoamperometric measurement was conducted, as depicted in Fig. 8(d), to evaluate the practical durability of the I & Ni-co-doped-$Co(OH)_2$ electrocatalyst for its OER performance. Throughout this experiment, a voltage in the range of 1.4 to 1.7 V (*versus* RHE) was implemented, and the ensuing iR-compensated current response was observed over a prolonged duration. The results of the multistep chronoamperometric measurement demonstrated the consistent and lasting response of the I & Ni-co-doped-$Co(OH)_2$ electrocatalyst in terms of its performance in the OER process. A prolonged duration of electrolysis was conducted with a consistent overpotential and current density to assess its stability. The results of this study indicated that the prepared electrode demonstrated remarkable conductivity, mechanical strength, and mass transfer characteristics. This was demonstrated by the slight variation observed in both the overpotential and current density over an extended period. The aforementioned properties show interesting significance in practical implementations owing to their ability to ensure lasting reliability of the electrocatalyst under the operational conditions. After the stability testing, the LSV curve of the electrocatalyst, specifically I & Ni-co-doped-$Co(OH)_2$, was examined, and the results indicated a negligible increase in overpotential, as illustrated in the inset of Fig. 8(e).

3.9 HER performance

The HER activity was investigated using other electrode materials, including pure platinum, α-$Co(OH)_2$, Ni-doped-$Co(OH)_2$, and I & Ni-co-doped-$Co(OH)_2$. The LSV curves and corresponding Tafel slopes of all the synthesized materials are shown in Fig. 9. The overpotential required for the pure platinum electrode to attain a current density of 10 mA cm^{-2} was found to be 130 mV, with a Tafel slope of 76 mV dec^{-1}. The mechanism of the HER on platinum involves the Volmer step, where water molecules adsorb on the platinum surface and undergo dissociation into hydrogen ions and electrons. Subsequently, the Tafel step occurs, where the adsorbed hydrogen atoms combine to form hydrogen gas. The Tafel slope of 76 mV dec^{-1} indicates a fast reaction rate on the platinum electrode.

In the case of α-$Co(OH)_2$, it required an overpotential of 337 mV to achieve the required current density, and its Tafel slope was measured to be 170 mV dec^{-1}. The higher overpotential and steeper Tafel slope observed for α-$Co(OH)_2$ indicate slower reaction kinetics compared to platinum. Alternatively, Ni-doped-$Co(OH)_2$ showed an enhanced performance with an overpotential of 284 mV and a Tafel slope of 124 mV dec^{-1}. The lower Tafel slope compared to α-$Co(OH)_2$ suggests improved reaction kinetics. The introduction of nickel dopants in α-$Co(OH)_2$ provides sites that promote both water adsorption and subsequent hydrogen gas formation.

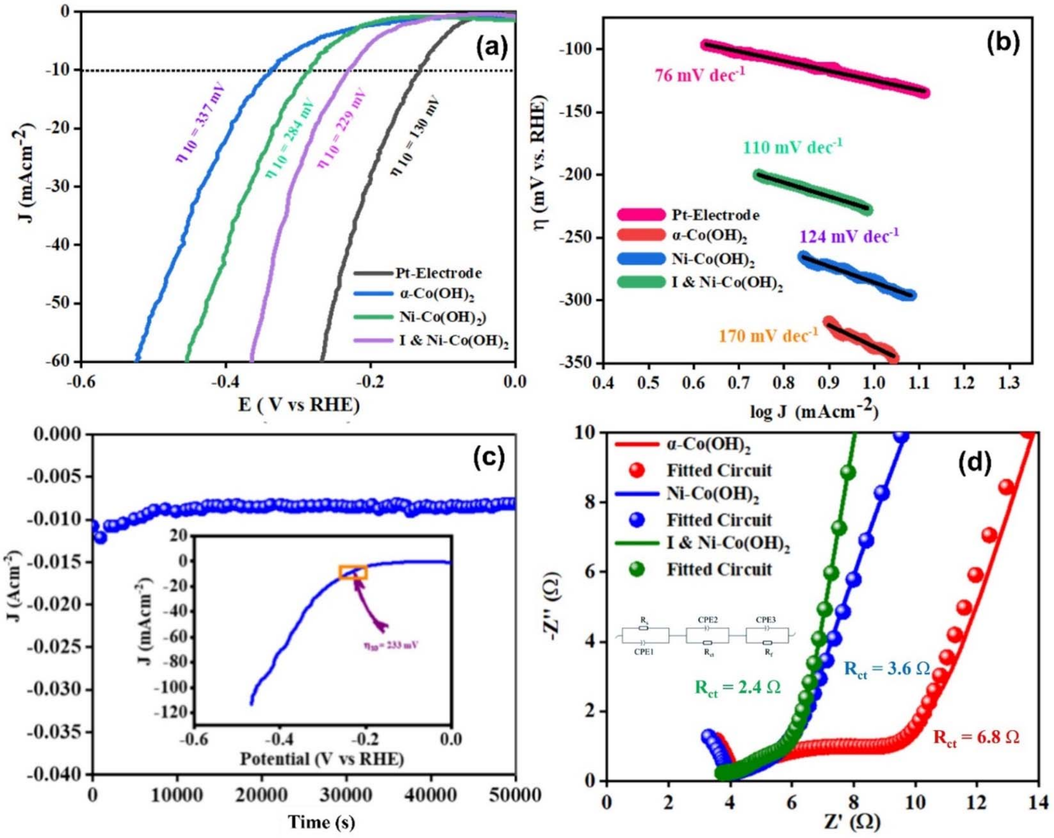

Fig. 9 HER LSV curves (a) and Tafel slopes (b) of different electrocatalysts tested in 1 M KOH alkaline aqueous solution using a 5 mV s^{-1} scan rate. (c) Prolonged duration chronoamperometric analysis and inset showing post-LSV analysis after the stability testing. EIS spectra (d) of electrocatalysts, including α-$Co(OH)_2$, Ni-doped-$Co(OH)_2$, and I & Ni-co-doped-$Co(OH)_2$.

Table 2 Experimental parameters for the HER assessment of α-$Co(OH)_2$, Ni-doped-$Co(OH)_2$, and I & Ni co-doped-$Co(OH)_2$

S. No.	Material	HER overpotential (mV)	Tafel slope (mV dec^{-1})	R_{ct} (Ω)
1	α-$Co(OH)_2$	337	170	6.8
2	Ni–$Co(OH)_2$	284	124	3.6
3	I & Ni–$Co(OH)_2$	229	110	2.4

The α-$Co(OH)_2$ co-doped with iodine and nickel demonstrated a catalytic performance with the lowest overpotential value of 229 mV and Tafel slope of 110 mV dec^{-1}, suggesting the greatest improvement in the kinetics of the reaction. The incorporation of iodine and nickel dopants in the structure of α-$Co(OH)_2$ increased the number of electrochemically active sites. Further, the HER stability of α-$Co(OH)_2$ co-doped with iodine and nickel was also considered in terms of chronoamperometric analysis. The observed current density was monitored, which remained almost uniform throughout the experiment, suggesting the excellent conductivity, mechanical strength, and efficient mass transfer properties of the material. The stability testing provided additional confirmation of the remarkable performance of α-$Co(OH)_2$ co-doped with I and Ni. This was evidenced by the cathodic LSV curve, which displayed a negligible increase in overpotential. This observation is depicted in the inset of Fig. 9(c). The exceptional stability demonstrated by I & Ni-co-doped-$Co(OH)_2$ underscores its considerable promise as a highly favorable electrocatalyst for sustainable and efficient hydrogen evolution reactions. All the HER experimental parameters are presented in Table 2.

The electrochemical impedance spectroscopic (EIS) approach was also applied to examine the inherent kinetics of electrochemical activity across the electrocatalysts. The application of this methodology provides a significant understanding of the electrochemical mechanisms occurring at the boundary linking the electrode and electrolyte through the analysis of the impedance reaction of the system upon a minor sinusoidal disturbance. The modified Randle's circuit was utilized for the fitting process of the EIS spectra. The circuit design employed for this purpose is illustrated in Fig. 9(d). Electrodes based on CFC materials demonstrate the presence of several resistance components, including solution resistance (R_S), charge transfer resistance (R_{CT}), and thin-film resistance (R_F), in the efficiency and effectiveness of different electrocatalysts in facilitating electrochemical activity.[35] I & Ni-co-doped-$Co(OH)_2$ (Fig. 9) exhibited the smallest arc radius among the electrocatalysts, thereby implying its lowest resistance values. The results indicate that the electrode composed of I & Ni-co-doped-$Co(OH)_2$ exhibits a notable reduction in charge transfer resistance measured at 2.4 Ω in contrast to the electrodes composed of either α-Co(OH)$_2$ or Ni-doped-Co(OH)$_2$. The I & Ni co-doped-Co(OH)$_2$ electrode demonstrated remarkable functionality because of its charge-trapping phenomenon, higher carrier concentration, and lower flat-band potential. The abovementioned factors improved the electron transfer at the electrode–electrolyte interface, leading to an enhancement in the electrocatalytic processes.[64] In addition, the exchange current densities for α-Co(OH)$_2$, Ni-doped-Co(OH)$_2$, and I & Ni-co-doped-Co(OH)$_2$ were also calculated. Among the electrocatalysts, the I & Ni-co-doped-Co(OH)$_2$ electrode demonstrated the largest exchange current density (2.67 mA cm^{-2}), which is attributed to its enhanced electrochemical activity and better charge transfer at the electrode–electrolyte interface.

4 Conclusions

In summary, the current study examined the electrocatalytic properties α-Co(OH)$_2$, Ni-doped-Co(OH)$_2$ and I & Ni-co-doped-Co(OH)$_2$ as electrode materials for energy conversion and storage. The results proved the excellent potential of these electrode materials. The pseudocapacitive behavior of the materials was observed by cyclic voltammetry measurements and their charge storage was followed by combination of both diffusion and capacitive-controlled processes. Furthermore, the specific capacitance of I & Ni-co-doped-Co(OH)$_2$ was calculated to be 1277 F g^{-1} by galvanostatic charge–discharge measurements, which also showed notable stability and high coulombic efficiency retention for 3000 consecutive cycles.

The water-splitting performance of I & Ni-co-doped-Co(OH)$_2$ exhibited efficient catalysis for both OER and HER, as reflected in its anodic and cathodic LSV curves, respectively. Notably, co-doped-Co(OH)$_2$ exhibited a superior electrocatalytic performance compared to its counterparts. The co-doped-Co(OH)$_2$ catalyst achieved an anodic current density of 100 mA cm^{-2} at 310 mV and 200 mA cm^{-2} at 340 mV. The OER Tafel slope analysis indicated that although Ni-doping did not improve the kinetics, iodine and nickel co-doping remarkably lowered the Tafel slope, indicating improved reaction mechanisms. The multistep chronoamperometric study highlighted the long-term stability and reliability of the I & Ni-co-doped-Co(OH)$_2$ electrocatalyst, demonstrating its practical viability for efficient energy conversion applications.

Noticeably, pure platinum exhibited the lowest HER overpotential (130 mV) and a smallest HER Tafel slope (76 mV dec^{-1}), signifying its efficient kinetics linked to the Volmer and Tafel steps. In contrast, α-Co(OH)$_2$ necessitated a higher HER overpotential (337 mV) and steeper Tafel slope (170 mV dec^{-1}), indicating its slower kinetics due to limitations in the reaction steps. Ni-doped-Co(OH)$_2$ displayed improved HER kinetics (284 mV and 124 mV dec^{-1}) due to the presence of additional active sites, facilitating the Volmer and Tafel steps, respectively. Remarkably, I & Ni-co-doped Co(OH)$_2$ exhibited a superior catalytic performance with the lowest HER overpotential (229 mV) and favorable Tafel slope (110 mV dec^{-1}) due to its enhanced electrochemical properties. Moreover, the extensive stability assessment of I & Ni-co-doped-Co(OH)$_2$ confirmed its robustness over prolonged HER, emphasizing its potential as a reliable electrocatalyst for sustainable and efficient hydrogen evolution. The aforementioned findings not only make a valuable contribution to the progress of energy conversion and storage technologies but also offer potential solutions to significant obstacles in the field of sustainable energy consumption.

Conflicts of interest

There are no conflicts of interest to declare.

Acknowledgements

The researchers wish to extend their sincere gratitude to the Deanship of Scientific Research at the Islamic University of Madinah for the support provided to the Post-Publishing Program. Prof. Dr Sonia Zulfiqar is highly thankful for the support provided by the Statutory City of Ostrava, Czechia through the Research Grant "Global Experts" and to the American University in Cairo, Egypt for using STRC facilities. Profs. Cochran and Zulfiqar are grateful for the TEM imaging provided by Dr Tracey Stewart of the Roy J. Carver High Resolution Microscopy Facility and for the XPS measurements provided by Dr Dapeng Jing of the Materials Analysis and Research Laboratory of the Iowa State University Office of Biotechnology. Profs. Cochran and Zulfiqar are grateful to the National Science Foundation for financial support through research grants NSF-2113695, NSF-2218070 and NSF-2242763. Authors are also thankful to the Institute of Chemistry, BJ Campus, The Islamia University of Bahawalpur (Pakistan).

References

1 X. Zheng, C. Han, C.-S. Lee, W. Yao, C. Zhi and Y. Tang, Materials challenges for aluminum ion based aqueous energy storage devices: Progress and prospects, *Prog. Mater. Sci.*, 2024, **143**, 101253.

2 M. Mukhtar Sirati, S. Sirati, U. Amara, A. Hussain, D. Hussain, M. Hanif, *et al.*, Samarium-based metal organic frameworks as high performance electrocatalyst for alkaline water splitting, *Fuel*, 2024, **362**, 130812.

3 M. Afaq, A. BaQais, E. W. Cochran, S. Zulfiqar, M. A. Amin, M. Shahid, *et al.*, Fabrication of $Ni_2O_2(OH)$/CNTs-based electrocatalyst for efficient bifunctional electrocatalytic water splitting, *Int. J. Hydrogen Energy*, 2024, **60**, 601–610.

4 S. Rafiq, M. Aadil, M. F. Warsi, S. Yousaf, M. T. Alotaibi, S. M. El-Bahy, *et al.*, NiO nanoparticles and their nanohybrid with flat rGO sheets: As an ideal electroactive material for hybrid capacitor applications, *Ceram. Int.*, 2022, **48**, 14596–14605.

5 S. Rafiq, A. K. Alanazi, S. Bashir, A. Y. Elnaggar, G. A. M. Mersal, M. M. Ibrahim, *et al.*, Optimization studies for nickel oxide/tin oxide (NiO/Xg SnO$_2$, X: 0.5, 1) based heterostructured composites to design high-performance supercapacitor electrode, *Phys. B*, 2022, **638**, 413931.

6 S. Yousaf, M. Aadil, S. Zulfiqar, M. F. Warsi, P. O. Agboola, M. F. Aly Aboud, *et al.*, Hierarchically porous CuO microspheres and their r-GO based nanohybrids for electrochemical supercapacitors applications, *J. Mater. Res. Technol.*, 2020, **9**, 14158–14167.

7 J. Wang, Z. Pan, Y. Wang, L. Wang, L. Su, D. Cuiuri, *et al.*, Evolution of crystallographic orientation, precipitation, phase transformation and mechanical properties realized by enhancing deposition current for dual-wire arc additive manufactured Ni-rich NiTi alloy, *Addit. Manuf.*, 2020, **34**, 101240.

8 T. Abdullah, S. I. Shamsah, I. A. Shaaban, M. Akhtar and S. Yousaf, Engineering energy storage properties of rGO based Fe_2O_3/CuO/PANI quaternary nanohybrid as an ideal electroactive material for hybrid supercapacitor application, *Synth. Met.*, 2023, **299**, 117472.

9 S. Yousaf, S. Zulfiqar, M. Shahid, A. Jamil, I. Shakir, P. O. Agboola, *et al.*, Electrochemical energy storage properties studies of $Cu_{0.2}Ni_{0.8}O$-Reduced graphene oxide nano-hybrids, *Ceram. Int.*, 2020, **46**, 14304–14310.

10 S. Manzoor, T. Munawar, S. Gouadria, M. Sadaqat, A. G. Abid, A. Munawar, *et al.*, Nanopetals shaped CuNi alloy with defects abundant active surface for efficient electrocatalytic oxygen evolution reaction and high performance supercapacitor applications, *J. Energy Storage*, 2022, **55**, 105488.

11 A. I. Osman, N. Mehta, A. M. Elgarahy, M. Hefny, A. Al-Hinai, AaH. Al-Muhtaseb, *et al.*, Hydrogen production, storage, utilisation and environmental impacts: a review, *Environ. Chem. Lett.*, 2022, **20**, 153–188.

12 M. Afaq, M. Shahid, I. Ahmad, S. Yousaf, A. Alazmi, M. H. H. Mahmoud, *et al.*, Large-scale sonochemical fabrication of a Co_3O_4–$CoFe_2O_4$@MWCNT bifunctional electrocatalyst for enhanced OER/HER performances, *RSC Adv.*, 2023, **13**, 19046–19057.

13 S. H. Gillani, M. Sohail, L. Abu El Maati, R. Altuijri, R. Zairov, M. F. Nazar, *et al.*, An efficient NiO/NiS/NiP heterostructure catalyst for oxygen evolution reaction, *J. Alloys Compd.*, 2024, **976**, 172931.

14 F. Zhao, B. Wen, W. Niu, Z. Chen, C. Yan, A. Selloni, *et al.*, Increasing Iridium Oxide Activity for the Oxygen Evolution Reaction with Hafnium Modification, *J. Am. Chem. Soc.*, 2021, **143**, 15616–15623.

15 M. Hassan, M. M. Baig, S. Yousaf, M. Faheem, A. Hussain, B. Niaz, *et al.*, Efficient water splitting catalyst: Low-temperature selenization of Co and Ni hydroxide nanosheets on carbon cloth for enhanced electro-catalytic activity, *Diamond Relat. Mater.*, 2023, **139**, 110298.

16 S. Wang, A. Lu and C.-J. Zhong, Hydrogen production from water electrolysis: role of catalysts, *Nano Convergence*, 2021, **8**, 4.

17 X. Tian, Y. Zhao, T. Gu, Y. Guo, F. Xu and H. Hou, Cooperative effect of strength and ductility processed by thermomechanical treatment for Cu–Al–Ni alloy, *Mater. Sci. Eng. A*, 2022, **849**, 143485.

18 M. Liu, J. Balamurugan, T. Liang and C. Liu, Mechanism of electrocatalytic CO_2 reduction reaction by borophene supported bimetallic catalysts, *J. Colloid Interface Sci.*, 2024, **659**, 959–973.

19 Y. Zhao, Co-precipitated Ni/Mn shell coated nano Cu-rich core structure: A phase-field study, *J. Mater. Res. Technol.*, 2022, **21**, 546–560.

20 G. Zhao, J. Ding, J. Ren, Q. Zhao, C. Mao, K. Wang, *et al.*, Understanding the role of transition metal single-atom electronic structure in oxysulfur radical-mediated oxidative degradation, *Environ. Sci. Ecotechnology*, 2024, **20**, 100405.

21 Y. Zhao, Stability of phase boundary between L12-Ni3Al phases: A phase field study, *Intermetallics*, 2022, **144**, 107528.

22 M. Sohail, M. Ayyob, A. Wang, Z. Sun, L. A. El Maati, R. Altuijri, *et al.*, An efficient Fe_2Se_3/Fe_2O_3 heterostructure electrocatalyst for oxygen evolution reaction, *Int. J. Hydrogen Energy*, 2024, **52**, 1290–1297.

23 N. A. Khan, I. Ahmad, N. Rashid, S. Hussain, R. Zairov, M. Alsaiari, *et al.*, Effective CuO/CuS heterostructures catalyst for OER performances, *Int. J. Hydrogen Energy*, 2023, **48**, 31142–31151.

24 Y. Zhao, Y. Sun and H. Hou, Core-shell structure nanoprecipitates in Fe-xCu-3.0Mn-1.5Ni-1.5Al alloys: A phase field study, *Prog. Nat. Sci.: Mater. Int.*, 2022, **32**, 358–368.

25 N. A. Khan, I. Ahmad, N. Rashid, M. N. Zafar, F. K. Shehzad, Z. ullah, *et al.*, Enhanced electrochemical activity of Co_3O_4/Co_9S_8 heterostructure catalyst for water splitting, *Int. J. Hydrogen Energy*, 2022, **47**, 30970–30980.

26 C. Cai, S. Han, X. Zhang, J. Yu, X. Xiang, J. Yang, *et al.*, Ultrahigh oxygen evolution reaction activity in Au doped co-based nanosheets, *RSC Adv.*, 2022, **12**, 6205–6213.

27 M.-C. Sung, G.-H. Lee and D.-W. Kim, CeO_2/$Co(OH)_2$ hybrid electrocatalysts for efficient hydrogen and oxygen evolution reaction, *J. Alloys Compd.*, 2019, **800**, 450–455.

28 N. P. Dileep, T. V. Vineesh, P. V. Sarma, M. V. Chalil, C. S. Prasad and M. M. Shaijumon, Electrochemically Exfoliated β-$Co(OH)_2$ Nanostructures for Enhanced Oxygen Evolution Electrocatalysis, *ACS Appl. Energy Mater.*, 2020, **3**, 1461–1467.

29 S. Sriram, S. Mathi, B. Vishnu and J. Jayabharathi, Entwined $Co(OH)_2$ in Situ Anchoring on 3D Nickel Foam with Phenomenal Bifunctional Activity in Overall Water Splitting, *Energy Fuels*, 2022, **36**, 7006–7016.

30 J. Zhou, L. Jiang, C. Shu, L. Kong, I. Ahmad and Y.-N. Zhou, A Universal Strategy For N-Doped 2D Carbon Nanosheets With Sub-Nanometer Micropore For High-Performance Supercapacitor, *Energy Environ. Mater.*, 2021, **4**, 569–576.

31 S. Guan, J. Zhou, S. Sun, Q. Peng, X. Guo and B. Liu, Nonmetallic Se/N Co-Doped Amorphous Carbon Anode Collaborates to Realize Ultra-High Capacity and Fast Potassium Storage for Potassium Dual-Ion Batteries, *Adv. Funct. Mater.*, 2024, 2314890.

32 Y. Men, P. Li, J. Zhou, G. Cheng, S. Chen and W. Luo, Tailoring the Electronic Structure of Co2P by N Doping for Boosting Hydrogen Evolution Reaction at All pH Values, *ACS Catal.*, 2019, **9**, 3744–3752.

33 Y. Kou, J. Liu, Y. Li, S. Qu, C. Ma, Z. Song, *et al.*, Electrochemical Oxidation of Chlorine-Doped $Co(OH)_2$

Nanosheet Arrays on Carbon Cloth as a Bifunctional Oxygen Electrode, *ACS Appl. Mater. Interfaces*, 2018, **10**, 796–805.

34 H. Lee, X. Zhang, B. Kim, J.-H. Bae and J. Park, Effects of Iodine Doping on Electrical Characteristics of Solution-Processed Copper Oxide Thin-Film Transistors, *Materials*, 2021, **14**, 6118.

35 S. Yousaf, S. Zulfiqar, H. H. Somaily, M. F. Warsi, A. Rasheed, M. Shahid, *et al.*, An efficient and stable iodine-doped nickel hydroxide electrocatalyst for water oxidation: synthesis, electrochemical performance, and stability, *RSC Adv.*, 2022, **12**, 23454–23465.

36 J. Zhang, Z.-H. Huang, Y. xu and F. Kang, Hydrothermal Synthesis of Iodine-Doped Bi_2WO_6 Nanoplates with Enhanced Visible and Ultraviolet-Induced Photocatalytic Activities, *Int. J. Photoenergy*, 2012, **2012**, 915386.

37 S. Yousaf, K. M. Katubi, S. Zulfiqar, M. F. Warsi, Z. A. Alrowaili, M. S. Al-Buriahi, *et al.*, Modulating electronic and structural properties of NiCo- layered double hydroxide with iodine: As an efficient electrocatalyst for the oxygen evolution reaction, *Int. J. Hydrogen Energy*, 2023, **48**, 27201–27214.

38 G. Zeng, M. Liao, C. Zhou, X. Chen, Y. Wang and D. Xiao, Iron and nickel co-doped cobalt hydroxide nanosheets with enhanced activity for oxygen evolution reaction, *RSC Adv.*, 2016, **6**, 42255–42262.

39 M. A. Kamran, G. Nabi, A. Majid, T. Alharbi, M. Z. Iqbal and N. Arshid, Activation of infrared emission in (iodine, nickel) Co-Doped CdS nanobelts for solar cells and optoelectronic applications, *Phys. B*, 2020, **594**, 412328.

40 S. Zhang, X. Liu, Z. Li, L. Hao, P. Wang, X. Zou, *et al.*, Iron and Iodine Co-doped Triazine-Based Frameworks with Efficient Oxygen Reduction Reaction in Alkaline and Acidic Media, *ACS Sustain. Chem. Eng.*, 2019, **7**, 11787–11794.

41 D. Tai Dam and J.-M. Lee, Ultrahigh pseudocapacitance of mesoporous Ni-doped $Co(OH)_2$/ITO nanowires, *Nano Energy*, 2013, **2**, 1186–1196.

42 Z. Liu, R. Ma, M. Osada, K. Takada and T. Sasaki, Selective and Controlled Synthesis of α- and β-Cobalt Hydroxides in Highly Developed Hexagonal Platelets, *J. Am. Chem. Soc.*, 2005, **127**, 13869–13874.

43 J. Di, J. Chang and S. Liu, Recent progress of two-dimensional lead halide perovskite single crystals: crystal growth, physical properties, and device applications, *EcoMat.*, 2020, **2**, 12036.

44 M. del Arco, R. Trujillano and V. Rives, Cobalt–iron hydroxycarbonates and their evolution to mixed oxides with spinel structure, *J. Mater. Chem.*, 1998, **8**, 761–767.

45 C. Yu, J. Yang, C. Zhao, X. Fan, G. Wang and J. Qiu, Nanohybrids from NiCoAl-LDH coupled with carbon for pseudocapacitors: understanding the role of nano-structured carbon, *Nanoscale*, 2014, **6**, 3097–3104.

46 H. Chen, L. Hu, M. Chen, Y. Yan and L. Wu, Nickel–Cobalt Layered Double Hydroxide Nanosheets for High-performance Supercapacitor Electrode, *Materials*, 2014, **24**, 934–942.

47 T. Wang, S. Zhang, X. Yan, M. Lyu, L. Wang, J. Bell, *et al.*, 2-Methylimidazole-Derived Ni–Co Layered Double Hydroxide Nanosheets as High Rate Capability and High Energy Density Storage Material in Hybrid Supercapacitors, *ACS Appl. Mater. Interfaces*, 2017, **9**, 15510–15524.

48 Q. Han, S. Viswanathan, D. L. Spainhower and S. K. Das, The nature of surface cracking in direct chill cast aluminum alloy ingots, *Metall. Mater. Trans. A*, 2001, **32**, 2908–2910.

49 W. Liu, Z. Zhang, Y. Zhang, Y. Zheng, N. Liu, J. Su, *et al.*, Interior and Exterior Decoration of Transition Metal Oxide Through Cu^0/Cu^+ Co-Doping Strategy for High-Performance Supercapacitor, *Nano-Micro Lett.*, 2021, **13**, 61.

50 F. Duan, Y. Zheng and M. Chen, Flowerlike $PtCl_4/Bi_2WO_6$ composite photocatalyst with enhanced visible-light-induced photocatalytic activity, *Appl. Surf. Sci.*, 2011, **257**, 1972–1978.

51 J. Wang, T. Xie, Q. Deng, Y. Wang, Q. Zhu and S. Liu, Three-dimensional interconnected $Co(OH)_2$ nanosheets on Ti mesh as a highly sensitive electrochemical sensor for hydrazine detection, *New J. Chem.*, 2019, **43**, 3218–3225.

52 L. Wang, H. Zhang, Y. Li, S. Xiao, F. Bi, L. Zhao, *et al.*, Construction of bundle-like cobalt/nickel hydroxide nanorods from metal organic framework for high-performance supercapacitors, *J. Mater. Sci.: Mater. Electron.*, 2022, **33**, 10540–10550.

53 Z. Ai, M. Wang, Z. Zheng and L. Zhang, Doping iodine in CdS for pure hexagonal phase, narrower band gap, and enhanced photocatalytic activity, *J. Mater. Res.*, 2011, **26**, 710–719.

54 Y. Gogotsi, Energy storage wrapped up, *Nature*, 2014, **509**, 568–569.

55 M. A. M. Khan, W. Khan, M. Ahamed, J. Ahmed, M. A. Al-Gawati and A. N. Alhazaa, Silver-Decorated Cobalt Ferrite Nanoparticles Anchored onto the Graphene Sheets as Electrode Materials for Electrochemical and Photocatalytic Applications, *ACS Omega*, 2020, **5**, 31076–31084.

56 V. A. Jundale, D. A. Patil, G. Y. Chorage and A. A. Yadav, Mesoporous cobalt ferrite thin film for supercapacitor applications, *Mater. Today: Proc.*, 2021, **43**, 2711–2715.

57 B. Rani, A. K. Nayak and N. K. Sahu, Electrochemical supercapacitor application of CoFe2O4 nanoparticles decorated over graphitic carbon nitride, *Diamond Relat. Mater.*, 2021, **120**, 108671.

58 K. Chaudhary, S. Zulfiqar, H. H. Somaily, M. Aadil, M. F. Warsi and M. Shahid, Rationally designed multifunctional Ti_3C_2 MXene@Graphene composite aerogel integrated with bimetallic selenides for enhanced supercapacitor performance and overall water splitting, *Electrochim. Acta*, 2022, **431**, 141103.

59 G. Nabi, W. Raza, M. A. Kamran, T. Alharbi, M. Rafique, M. B. Tahir, *et al.*, Role of cerium-doping in $CoFe_2O_4$ electrodes for high performance supercapacitors, *J. Energy Storage*, 2020, **29**, 101452.

60 M. Anwar, E. W. Cochran, S. Zulfiqar, M. F. Warsi, I. Shakir and K. Chaudhary, In-situ fabricated copper-holmium co-doped cobalt ferrite nanocomposite with cross-linked graphene as novel electrode material for supercapacitor application, *J. Energy Storage*, 2023, **72**, 108438.

61 H. Fan, J. Jia, D. Wang, J. Fan, J. Wu, J. Zhao, *et al.*, High-valence Zr-incorporated nickel phosphide boosting

reaction kinetics for highly efficient and robust overall water splitting, *Chem. Eng. J.*, 2023, **455**, 140908.

62 D. Antipin and M. Risch, Calculation of the Tafel slope and reaction order of the oxygen evolution reaction between pH 12 and pH 14 for the adsorbate mechanism, *Electrochem. Sci. Adv.*, 2023, **3**, 2100213.

63 K. Xiang, J. Guo, J. Xu, T. Qu, Y. Zhang, S. Chen, *et al.*, Surface Sulfurization of NiCo-Layered Double Hydroxide Nanosheets Enable Superior and Durable Oxygen Evolution Electrocatalysis, *ACS Appl. Energy Mater.*, 2018, **1**, 4040–4049.

64 Y. Wang, Y.-Y. Zhang, J. Tang, H. Wu, M. Xu, Z. Peng, *et al.*, Simultaneous Etching and Doping of TiO_2 Nanowire Arrays for Enhanced Photoelectrochemical Performance, *ACS Nano*, 2013, **7**, 9375–9383.